PAPER

Discretized hexagonal boron nitride quantum emitters and their chemical interconversion

View the article online for updates and enhancements.

Discretized hexagonal boron nitride quantum emitters and their chemical interconversion

Daichi Kozawa[1,2,9]**, Sylvia Xin Li**[1,9]**, Takeo Ichihara**[1,3]**,
Ananth Govind Rajan**[1,4]**, Xun Gong**[1] **, Guangwei He**[1,9]**,
Volodymyr B Koman**[1]**, Yuwen Zeng**[1]**, Matthias Kuehne**[1]**, Kevin S Silmore**[1]**,
Dorsa Parviz**[1]**, Pingwei Liu**[1,5]**, Albert Tianxiang Liu**[1,6]**, Samuel Faucher**[1]**,
Zhe Yuan**[1]**, Jamie Warner**[7,8]**, Daniel Blankschtein**[1] **and Michael S Strano**[1,*]

[1] Department of Chemical Engineering, Massachusetts Institute of Technology, Cambridge, MA 02139, United States of America
[2] Quantum Optoelectronics Research Team, RIKEN Center for Advanced Photonics, Saitama 3510198, Japan
[3] Energy and System R&D Department, Chemistry and Chemical Process Laboratory, Corporate R&D, Asahi Kasei Corporation, Kurashiki, Okayama 7118510, Japan
[4] Department of Chemical Engineering, Indian Institute of Science, Bengaluru, Karnataka 560012, India
[5] College of Chemical and Biological Engineering, Zhejiang University, Hangzhou, Zhejiang Province 310027, People's Republic of China
[6] Department of Chemical Engineering, University of Michigan, Ann Arbor, MI 48109, United States of America
[7] Walker Department of Mechanical Engineering, The University of Texas at Austin, Austin, TX 78712, United States of America
[8] Materials Graduate Program, Texas Materials Institute, The University of Texas at Austin, Austin, TX 78712, United States of America

E-mail: strano@mit.edu

CrossMark

Abstract
Quantum emitters in two-dimensional hexagonal boron nitride (hBN) are of significant interest because of their unique photophysical properties, such as single-photon emission at room temperature, and promising applications in quantum computing and communications. The photoemission from hBN defects covers a wide range of emission energies but identifying and modulating the properties of specific emitters remain challenging due to uncontrolled formation of hBN defects. In this study, more than 2000 spectra are collected consisting of single, isolated zero-phonon lines (ZPLs) between 1.59 and 2.25 eV from diverse sample types. Most of ZPLs are organized into seven discretized emission energies. All emitters exhibit a range of lifetimes from 1 to 6 ns, and phonon sidebands offset by the dominant lattice phonon in hBN near $1370 \, \mathrm{cm}^{-1}$. Two chemical processing schemes are developed based on water and boric acid etching that generate or preferentially interconvert specific emitters, respectively. The identification and chemical interconversion of these discretized emitters should significantly advance the understanding of solid-state chemistry and photophysics of hBN quantum emission.

Supplementary material for this article is available online

(Some figures may appear in colour only in the online journal)

---

[9] These authors contributed equally.
[*] Author to whom any correspondence should be addressed.

Introduction

hBN is a two-dimensional (2D) layered material that can be exfoliated or synthesized with a thickness of a single unit cell, providing molecularly thin dielectrics [1], chemically resistant coatings [2] and nanoporous membranes [3]. Since 2016, atomic defects in hBN exhibiting room-temperature single-photon emission [4] have been attracting tremendous research interest. Such unique photophysical properties are highly desirable for quantum computing and communications [5]. Compared to their bulk counterparts, 2D materials hosting single-photon sources benefit from higher light extraction efficiency, and easier integration with on-chip photonic [6] and optoelectronic devices [7].

A practical challenge lies in the difficulty of engineering emitting defects with deterministic photophysical properties. Recent advances in materials science have uncovered that the emission energy of hBN defects varies from sample to sample in a wide span, which has been observed in both photoluminescence (PL) [8, 9] and cathodoluminescence [10]. hBN emitters form either naturally in bulk crystals [11], or by postprocessing such as liquid exfoliation [12], electron beam radiation [13, 14], oxygen atom irradiation [15], oxygen plasma [16], and argon plasma with subsequent annealing [16]. The lack of modulating the emission wavelength in more diverse hBN samples urgently calls for a statistical spectroscopic investigation, which will deepen the fundamental understanding of the origin of hBN quantum emission and bridge the knowledge gap between different emitter-forming methods.

In this work, we carry out a comprehensive study using a variety of hBN samples with different layer thickness and various preparation methods including chemical vapor deposition (CVD) and liquid-phase exfoliation. A custom-built confocal spectroscopic microscope equipped with a piezoelectric stage enables the automation of collecting large numbers of PL spectra, where minimum manual operation is needed. To analyse the emission properties, we extract single, isolated zero-phonon lines (ZPLs) from more than 2000 spectra, with the assistance of a software tool we develop. A prominent feature of the ZPL ensemble is the quantization into six ubiquitous emission energies observed across diverse hBN samples. PL excitation, polarization, and time-resolved PL measurements are conducted for the six species of the emitters in detail. We also develop chemical etching schemes that allow an interconversion of different emitter species, which strengthens our conclusion that the emission energy distribution is discretized among hBN emitters. We additionally demonstrate that high-energy probe-tip ultrasonication produces the seventh emitter species, exhibiting isotropic polarization.

Results and discussions

Discretization of emission energies

For optical characterization, we first use multilayer liquid-exfoliated hBN as a model system. Liquid exfoliation produces multilayer hBN flakes with a lateral size of hundreds of nanometres, which are suspended in a water-ethanol mixture. These multilayer flakes were drop-casted onto SiO_2/Si substrates and annealed in Ar for 30 min (supplementary section 1). Optical micrographs show a representative area with multiple hBN flakes (figure 1(a)), whose thicknesses of 100–180 nm are obtained by atomic force microscopy (figure 1(b), a profile in figure S7, and statistics in figure S23). Using automated confocal spectroscopy (figure S1), the sample with hBN flakes is scanned, during which a PL spectrum is collected at each scanning step (supplementary section 2). Confocal (figure 1(c)) and hyperspectral (figure S2) PL maps reveal that the emission energy of hBN flakes spans a wide range. We observe distinctive ZPLs and phonon sidebands of the first and second order with the distance of approximately 170 meV between them (figure 1(d)), which is consistent with the dominant phonon mode [17] in the Raman response of hBN (figure S3). In a Hanbury Brown and Twiss interferometry measurement, the second-order photon correlation function exhibits a clear dip below 0.5 at zero delay time (figure 1(e)), which is characteristic of photon antibunching [5]. Such photon antibunching effects are observed among emitters with a wide range of emission energies from $\sim$1.6 to $\sim$2.3 eV in liquid-exfoliated hBN (figure S4).

Emission energies from various sample preparation methods are now studied by collecting the set of PL spectra (figure S6). We extract peak centres by fitting a Lorentzian function to a ZPL. The emission energy distribution of 264 ZPLs from liquid-exfoliated hBN is plotted in a histogram (figure 1(f)). The emission energies appear to be discretized within approximately 40 meV linewidth and are organized into six modes (figure 1(f)). We then compare the emission distributions of different hBN samples such as multilayer CVD-grown hBN (figure 1(g)), monolayer CVD-grown hBN (figure 1(h) from Graphene Supermarket with atomic force micrograph in figures S8, S9 from Grolltex), multilayer liquid-exfoliated hBN modified by chemical etching (figure 1l), and emission data obtained from a recent cathodoluminescence study [10] (figure 1(m)). We also observe a new emitter species P_7 at 1.79 eV that exhibits distinct isotropic polarization by applying probe-tip ultrasonication to multilayer liquid-exfoliated hBN (figure 1(n)), which we will discuss in detail later. Notably, the discretization of emission energies remains almost invariant in all cases, which is compatible with clustering of emission energies reported on C-doped hBN [18–20] and B-gettered hBN [21] as well as as-prepared hBN [22–24].

Regarding the distribution of emitter species, P_2 and P_3 are the major species in both liquid-exfoliated (figure 1(i)), multilayer CVD hBN (figure 1(j)), and hBN in literature (figure S10). P_3 is the main emission species in monolayer CVD hBN from two different vendors, as shown in figure 1(k) (Graphene Supermarket) and figure S9 (Grolltex, supplementary section 3). Since we use 532 nm green laser as the excitation source, the observation of more P_2 and P_3 emitters could be preferentially populated due to the resonant phonon effect [25]. We recognize that excitation in UV [26, 27] and blue ranges [28] allows for observing ZPLs in
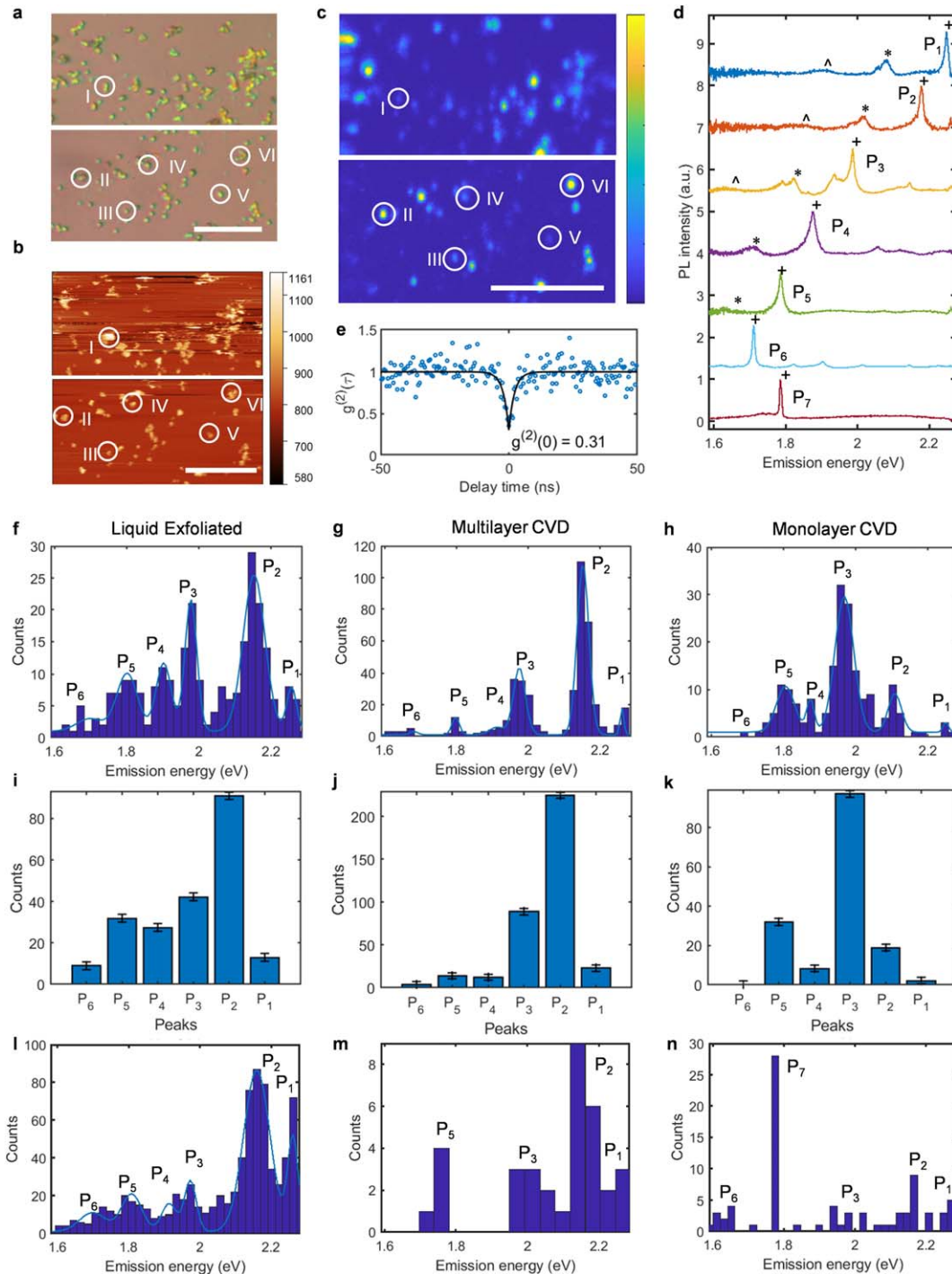
Figure 1. Optical (a) and atomic force micrographs (b) for multilayer hBN flakes from liquid-phase exfoliation. (c) Confocal PL imaging of these hBN flakes, where the color bar corresponds to the normalized intensity, with blue as 0 and yellow as 1. Scale bars in (a), (b) and (c) correspond to 10 μm. (d) Zero-phonon lines (ZPLs) between 1.6 and 2.2 eV. Spectra I–VI are obtained at the spots highlighted in (a)–(c), and ZPLs (+), one-phonon (*) and two-phonon (ˆ) sidebands are observed. (e) Photon correlation curve for P_2 in multilayer liquid-exfoliated hBN with a fit by a simple two-level model showing photon antibunching. (f) Histogram of emission energies from multilayer liquid-exfoliated hBN, showing six discretized modes at P_1 (2.25 $\pm$ 0.03 eV), P_2 (2.15 $\pm$ 0.06 eV), P_3 (1.98 $\pm$ 0.04 eV), P_4 (1.90 $\pm$ 0.04 eV), P_5 (1.81 $\pm$ 0.04 eV), and P_6 (1.69 $\pm$ 0.06 eV) obtained with multiple Gaussian fits (supplementary information section 4). Histograms of multilayer (g) and monolayer (h) hBN grown by CVD show the same discretized distribution into six clusters. Light-blue lines are fits with six-Gaussian function. Histograms of population for P1 through P6 obtained by integration of each Gaussian function corresponding to P_i ($i = 1, 2, \ldots, 6$) for (i) liquid-exfoliated hBN, (j) multilayer, and (k) monolayer hBN. Error bars are the standard deviations of the Gaussian fits. (l) Summary of cumulative boric acid etching to liquid-exfoliated hBN for 1 to 30 min (m) Histogram reproduced from the cathodoluminescence study of liquid-exfoliated hBN [10], showing the similar discretized modes of P_1, P_2, P_3, and P_5. (n) Tip-probe ultrasonication of liquid-exfoliated hBN produces a new emitter species labeled as P_7 at 1.79 eV.

higher energies. Although the higher energy excitation could alter the distribution, we focus on the detection range from ∼1.6 to ∼2.3 eV in this study.

From the Gaussian fits to histograms in figures 1(f)–(h), variability of emission energies for each species can be also extracted. Here we emphasize that the difference of emission energies between neighbouring species of P_i and P_{i+1} ($i = 1$, 2, …, 5) ranges from 80 to 170 meV. Although one may recognize the difference originate from strain and electric field, the energy differences are larger than the reported maximum tuning emission energy of 65 meV by strain [29] and 50 meV by electric field [30]. Moreover, the tuning of emission energy from strain [31–35] should be continuous, and not be discretized [31], indicating these effects could not induce the discretization of emission energies across such a wide range. The strain and the electric field are more likely to contribute to the variation of emission energy within each species because an average linewidth in the Gaussian fits of 57 ± 21 meV is comparable with the tuning range [29, 30]. We note that the variability within emission species also coincides with the temporal, stochastic spectral fluctuations in the emission energy of emitters in multilayer CVD hBN, which is discussed in supplementary sections 7 and 8.

Photophysical properties of each emitter species

We now proceed to investigate photophysical properties of each emitter species by PL excitation spectroscopy to obtain insight into the electronic structures [26, 36]. Multilayer liquid-exfoliated sample is used, where emitters are photo-stable within the data collection time of 300 s (figure S11, supplementary section 5). Excitation spectra of P_1 through P_6 reveal peaks that are notably broader than the ZPLs (figure 2(a)). The broad peaks in the excitation spectra are assigned to phonon side bands (PSBs) (figure 2(b)) which is consistent with [37]. Note that the energy difference between the ZPLs and the first PSBs is between 158 and 166 meV for P_1 through P_5 (PL of PSBs for P_6 are beyond the detection range), as tabulated in table S1. These values of energy difference correspond to phonon energies of 1274 to 1339 cm^{-1} in wavenumber (figure 2(c)), which is comparable to the typical Raman mode in hBN [17] observed at 1367.5 cm^{-1} (figure S3).

It is also possible to study dielectric environments of from PL lifetime obtained by time-resolved PL measurements. We compare PL lifetimes among different emitter species for multilayer liquid-exfoliated hBN and monolayer CVD hBN (figure 2(d), typical PL decay curve for P_2 in figure S12, supplementary section 6). The lifetime is found to be independent of the emitter species in both multilayer liquid-exfoliated and monolayer CVD hBN (figure 2(d)). Monolayer hBN has a shorter average lifetime of 1.4 ± 0.47 ns than that of 2.5 ± 1.3 ns in multilayer hBN. This effect could be amplified in atomically thin materials, since the emitting structures are more likely to be exposed to the external environment [38]. For monolayer hBN, emitters must stay in contact with the external atmosphere and the substrate. Similarly, for multilayer hBN, emitters located near the top

surface or the bottom substrate can be quenched due to interactions with external gas or solid-state energy sinks. By contrast, emitters embedded within the crystal are in better encapsulation, and thus should exhibit longer lifetimes. As a result, the broad lifetime distribution in multilayer samples can be attributed to emitters located in different layers of hBN.

To better understand the dipole nature of each emitter, we investigate the polarization dependence of ZPLs for P_1 through P_6 in multilayer liquid-exfoliated hBN. Excitation and emission polarization measurements of emitters show a two-fold symmetry for all the emitter species as presented in figure 2(e). Consistent with previous reports [4, 39–42], the observed two-fold symmetry indicates that the excitation in liquid-exfoliated hBN is a single, linearly polarized dipole transition, independent of the wide range of emission energies. We also observe lower polarization degree in the excitation than emission in most emitters (figure 2(e)). The relatively low polarization degree in excitation could originate from excitation of multiple dipoles whereas the higher polarization in emission could be attributed to relaxation to lowest states accompanied with emission. We also note that asymmetric polarization degree in figure 2(e) may be artefacts of the optical setup. However, the obtained polarization angles are accurate because the intensity maxima are still on the same axis.

The excitation and emission polarization dependence shows angle difference, and more data of polarization angle differences are collected for all the emitter species. The excitation and emission polarization angles are rarely aligned, and the angle difference varies from 0 to 90 degree across a wide emission energy range of P_1 through P_6 (figure 2(f)). In contrast to the previous reported results at cryogenic temperatures,[30] the angle difference of P_1 (2.25 ± 0.05 eV) and P_2 (2.15 ± 0.05 eV) emitters (with emission energies close to the 2.33 eV excitation) are not clustered near 0 degree at room temperature, but instead around 80 degree (figure 2(f)).

Preferential interconversion among different emitter species by chemical etching

We now turn to modifying the emitters' optical properties by boric acid etching (detailed in supplementary section 9, 10). We first focus on liquid-exfoliated hBN that is stable and non-blinking emitters and thus a model system for etching. Before and after boric acid etching, PL spectra for the same hBN flakes are taken and hyperspectral maps are constructed. Examples of such mapping in figure 3(a) show that the boric acid etching modulate the ZPL spatial distribution of each emitter species P_i ($i = 1, …, 6$). The hyperspectral maps are statistically analyzed by extracting point-to-point PL spectral change, and we find that the change in the spectra is mainly grouped into four categories: unchanged ZPLs (figure 3(b)), ZPLs disappearing and turning into non-emission modes (figure 3(c)), new ZPLs appearing from non-emitting regions (figure 3(d)), and interconversion from P_i to P_j ($i, j = 1, …, 6$) (figure 3(e)).
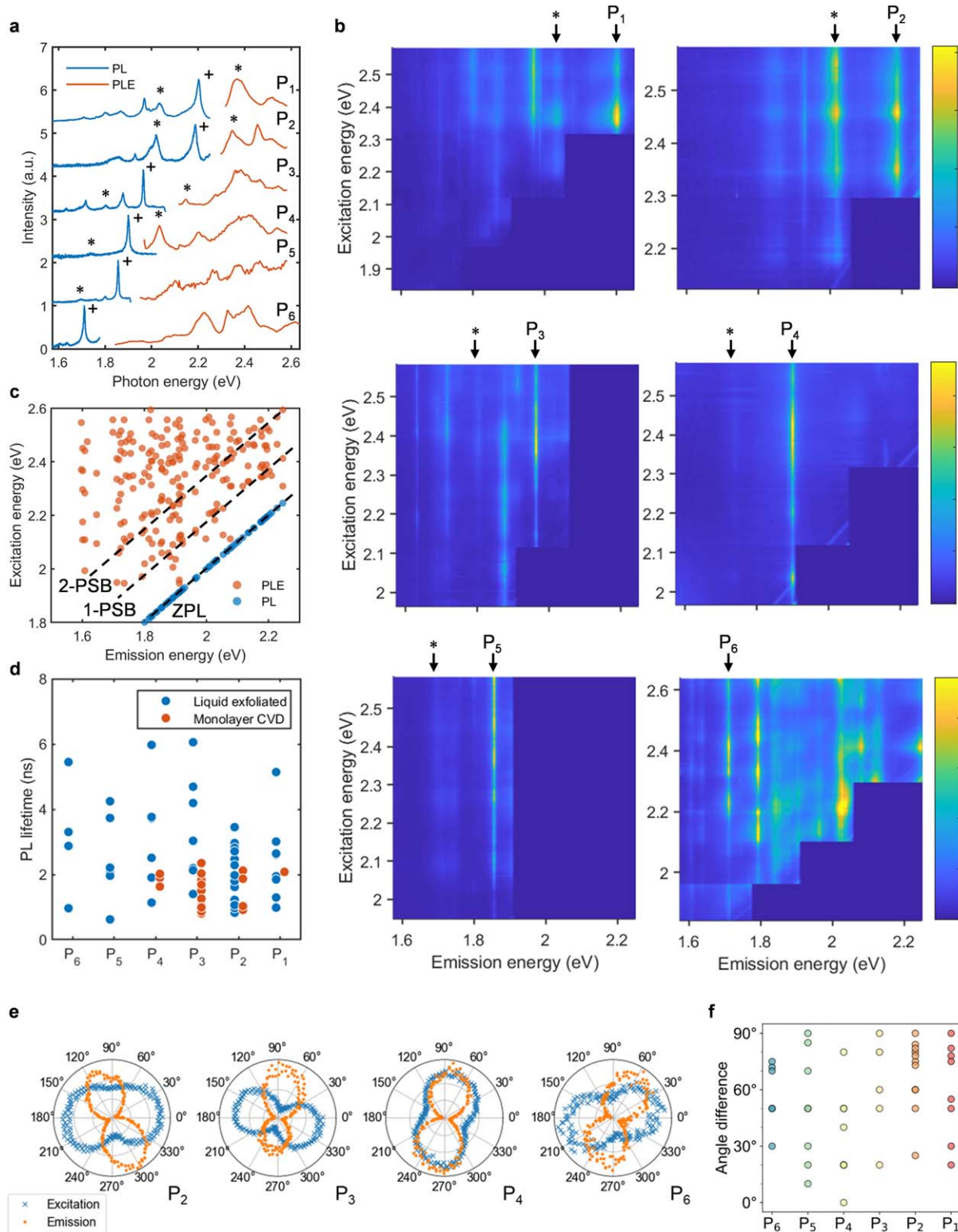
Figure 2. (a) PL and PLE spectra of multilayer liquid-exfoliated hBN for P_1 through P_6 showing different resonant energy to excitation, where the zero-phonon lines and phonon sidebands are labeled with '+' and '*,' respectively. (b) PLE maps of multilayer liquid-exfoliated hBN for P_1 through P_6, where zero-phonon line of P_i ($i = 1, \ldots, 6$) and first PSB (*) are indicated by arrows. The color bars in (b) correspond to the normalized intensity, with blue as 0 and yellow as 1. (c) Orange scatter plot is extracted from PL excitation profiles (PLE), and blue scatter plot is extracted from PL spectra. The dashed lines indicate zero-phonon line (ZPL), one-phonon sideband (1-PSB), and two-phonon sideband (2-PSB), respectively. (d) Average PL lifetime for multilayer liquid-exfoliated hBN and monolayer CVD hBN obtained by a fit of mono-exponential function. (e), Excitation (blue) and emission (orange) polarization dependent PL intensity in multilayer liquid-exfoliated hBN from representative P_2, P_3, P_4 and P_6 emitters, where the total rotation angle is 720° for each measurement. The angle difference between excitation and emission is summarized in a scatter plot (f), with emitter species of P_1 through P_6 corresponding to different emission energies.
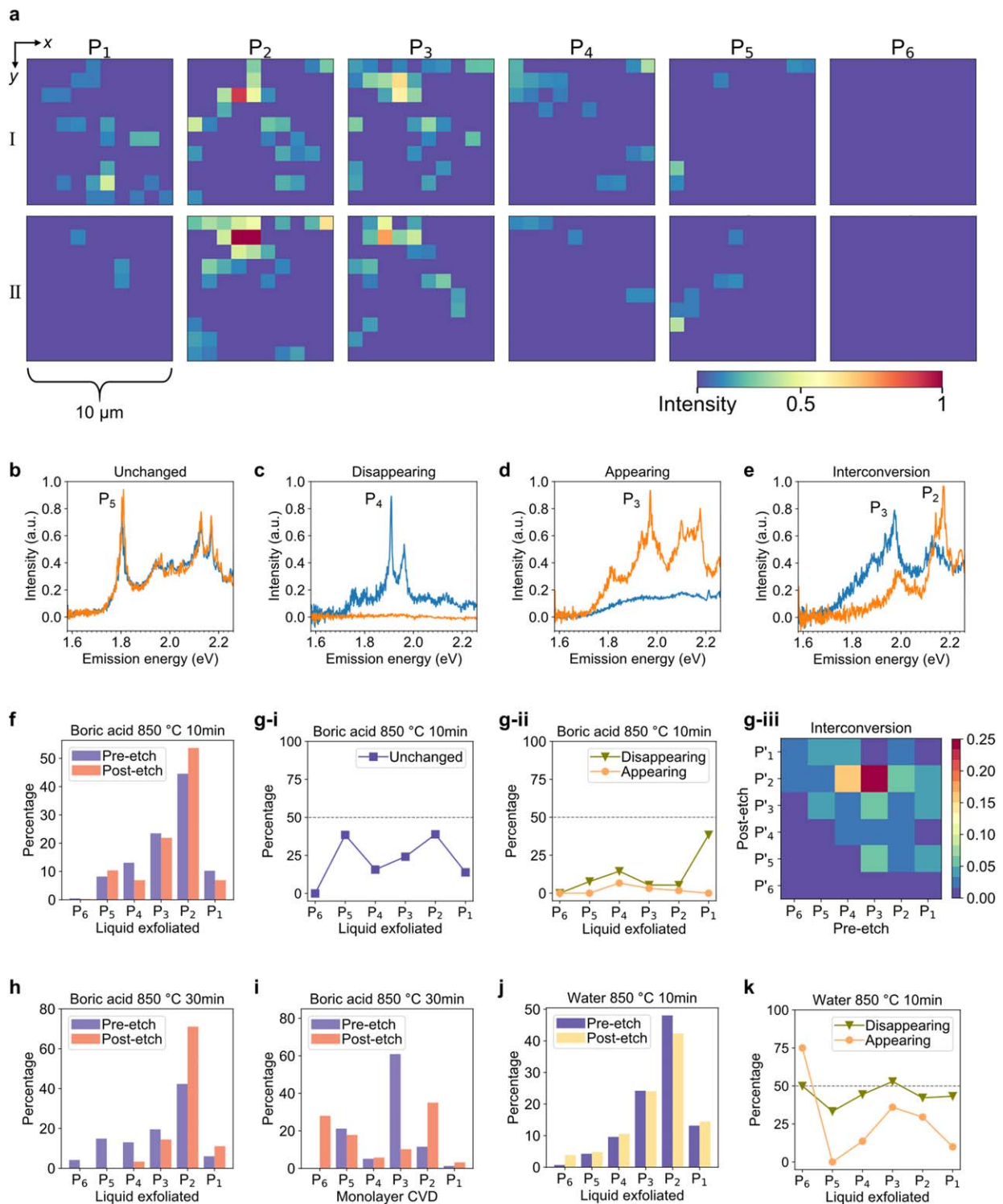
Figure 3. (a) Hyperspectral PL mapping of multilayer liquid-exfoliated hBN in the same region of 10×10 μm with 1-μm step, before (row I) and after (row II) boric acid etching at 850 °C for 10 min Each column corresponds to a specific P_i ($i = 1, \ldots, 6$). In each color map, *x*- and *y*-coordinates denote the location of an emitter, and the color of a pixel indicates the normalized intensity of a ZPL to the maximum intensity. Note that (a)–(g) are obtained from the same data set characterizing the boric acid etching. Typical spectral changes between pre-etch (blue) and post-etch (orange) measurements are shown in (b) unchanged, (c) disappearing of ZPLs into non-emitting mode, (d) appearing of new ZPLs from non-emitting region, and (e) interconversion of ZPLs. (f) Emitter species distributions of pre-etch and post-etch measurements are presented with the percentage of each emission species. Percentage of (g–i) unchanged, (g–ii) disappearing ZPLs, and (g–iii) interconverting of ZPLs for each emitting species. (h) Emitter species distribution before and after 30 min boric acid etching. (i) Distribution with 30 min boric acid etching of monolayer CVD hBN. (j) Distribution with water vapor etching of liquid-exfoliated hBN at 850 °C for 10 min (k) Percentage of disappearing ZPLs in the experiments of (j).

We now consider the first three cases including unchanged, disappearing, and appearing based on the statistical analysis. The distributions of the post- and pre-etch emitter species are presented in percentage of each species (figure 3(f)) and in count numbers (figure S19). The total distribution of P_2 shows that the percentage increases (figure 3(f)) while the point-to-point analysis shows that 40% of P_2 is unchanged (figures 3(g–i)) and less than 10% of P_2 is disappearing and appearing by the etching (figures 3(g–ii)). From these results, that boric acid etching rarely creates new emitters, and some emitters show interconversion.

We then consider the case of interconversion where one species is converted into another. Interconversion pathways between P_i ($i = 1, \ldots, 6$) and P_j ($j = 1, \ldots, 6$) are counted (summarized in figure S20) and probabilities of the interconversion are presented in a map (figures 3(g–iii)). The most probable pathway is P_3 converting into P_2. As shown in figure 3(e), the difference between P_3 and P_2 is approximately 200 meV, which is much larger than the maximum tuning limit of 65 meV or 50 meV by strain or electric field [29, 30]. In fact, an interconversion from P_4 to P_1 is also possible, where the emission energy changes approximately 350 meV. While we could not completely rule out the possibility of disappearing and appearing occurring at the same measurement spot, the probability of such events is enough low (figures 3(g–ii)).

Time evolution of the etching process should provide insight to the defect structure in terms of thermodynamics. By extending the boric acid etching time to 30 min (figure S21), we observe that the percentage of P_2 increases after etching (figure 3(h)), in agreement with the trend in shorter time etching (figure 3(f)). Interconversion from P_3 into P_2 is also observed by monolayer CVD hBN where P_3 decreases significantly and P_2 increases (figure 3(i)). In all three cases of boric acid experiments, P_2 becomes the dominant mode after etching. These results suggest that P_2 could originate from a more thermodynamically stable defect structure.

Etching process is investigated by comparing with water vapor etching that should show different chemistry. The percentage of each emitter species in the distribution does not change significantly after water vapor etching (figure 3(j)). Moreover, the main spectral change in the point-to-point analysis involves ZPLs disappearing i.e. converting into non-emission species and new ZPLs appearing from non-emitting regions (figure 3(k)). Water vapor etching deactivates approximately half of all existing emitters, with no obvious preference for a specific P_i ($i = 1, \ldots, 6$). We find that water vapor reduces large numbers of existing emitters and simultaneously generates new emitters, whereas boric acid prefers modifying existing emitters. It should be noted that the emission energy distribution remains discretized after both chemical etching processing (figure 1(l)). These results strengthen the assertion of a discretized emission energy distribution since the same emission species P_1 through P_6 are observed after chemical modifications.

One possible explanation is that water has a much smaller molecular size, and thus could intercalate between hBN layers more easily at high temperatures [43]. Although boric acid also release water, the water concentration during water vapor etching is relatively stable and uniform inside the quartz tube, reaching approximately 2 vol%. Accordingly, water vapor etching could correspond to a much faster etching kinetics. At high temperatures, boric acid [44] and water could both form hydroxyl radicals (•OH), thereby promoting the etching [45] of dangling bonds [46] and enlarging existing lattice vacancies. This etching process leads to the deactivation by water vapor etching, transforming into larger defects that are no longer emitting. Meanwhile, new defects could form due to water vapor etching, thus leading to the appearance of new emitters in previous non-emitting regions. According to the above analysis, it is highly likely that the structural origin of emitters is related to the vacancy size of defects.

It is also possible that non-emitting defects get activated by protonation and hydroxylation during etching [18, 46, 47]. These functionalization groups could provide an out-of-plane component to the defect structures, which could significantly change the photophysical properties of defects. Boric acid could induce oxygen-incorporated BN structures due to the strong B-O bonds sustained at high temperatures [18]. Note that in both boric acid and water vapor etching, no large amounts of additional elements are brought in, besides H, O, B only in boric acid, likely some C easily found in the environment, and possibly small amount of Si existing in the quartz tube of the furnace and the SiO_2 substrate. Yet the emission energies could be modulated significantly. It should be noted that thermal annealing alone, and a wide range of other processing conditions, do not alter the emitter population significantly (figure S22, supplementary section11). Consequently, in addition to the vacancy size, functionalization of vacancy edge atoms e.g. with -H and -OH as well as substitution of O and possibly C in the hBN lattice [18, 48] could play key roles in determining the photophysical properties of emitting defects.

Generating the seventh emitter species by ultrasonication

By using a harsher treatment method to liquid-exfoliated hBN, a previously unobserved emitter species is generated and characterized. Liquid-exfoliated hBN purchased from Graphene Supermarket is ultra-sonicated with a probe tip for up to 60 min, followed by annealing at 850 °C in Ar for 30 min The high-energy tip sonication significantly modifies the morphology of liquid-exfoliated hBN where hBN flakes become thinner and smaller (figure S23) but the same chemical components (figure S24, supplementary section 12). The sonicated hBN shows narrower ZPLs than as-prepared hBN by 4 meV and broad PLE peak spanning from 2.2 to 2.28 eV with no clear PSBs (figures 4(a) and S25). The emission energy is centered at 1.79 eV lower than P_5 by 20 meV, and the new emitter species is labelled as P_7. As the sonication time increases, the new P_7 becomes dominant (figure 4(b)). We find that the probability of observing P_7 increases up to 50% with ultra-sonication time extending to 60 min (figure 4(b)), while the percentage of P_2 and P_3 species consistently decrease.
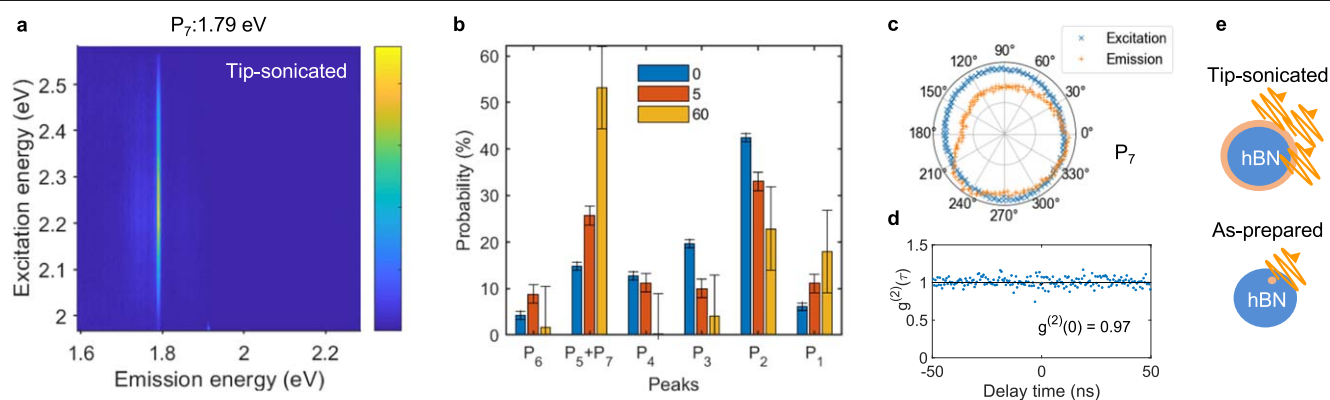
Figure 4. (a) PL excitation map of liquid-exfoliated hBN that are processed with high-energy tip-sonication, exhibiting new emission at 1.79 eV labeled as P_7. (b) Distributions of emitter species show the evolution of P_7, with tip-sonication time ranging from 0 to 60 min (c) Angular dependent PL intensity reveals that P_7 exhibits isotropic polarization in excitation and near-isotropic in emission, in contrast to the two-fold symmetry in other emitter species of P_1 through P_6. (d) Second-order photon correlation function of P_7 does not show a clear dip. (e) Schematic of multiple emitters forming along the edge of an hBN flake after tip-sonication (top), and a single emitter in as-prepared hBN (bottom).

The nature of the dipole for P_7 is characterized by polarization-dependent PL and photon correlation measurements. Polar plots for P_7 exhibit an isotropic polarization (figure 4(c)) in excitation and near-isotropic in emission, in contrast to the two-fold linear polarization of previously discussed P_1 through P_6. Here we note that boric acid and water vapor etching do not change the two-fold linear polarization of emitters in liquid-exfoliated hBN. The second-order photon correlation measurement reveals that P_7 is not a single-photon emitter (figure 4(d)). During ultra-sonication treatment, the acoustic cavitation from micro-bubble collapse is known to generate a destructive water jet, and induce high temperatures up to 5000 °C in local regions [48]. Additionally, hBN flakes are surrounded by water molecules, which could functionalize flake edges as well as vacancy edges during the sonication process. We therefore propose that tip sonication could generate P_7 emitters along the edge of a flake (figure 4(e)), leading to the superposition of multiple mirror-symmetric dipoles, which could explain the observed isotropic angular dependence of polarization in both excitation and emission.

Conclusion

In conclusion, we have presented a systematic statistical study of diverse hBN emitters by analysing more than 2000 spectra, with the automated spectroscopic approach we develop. We have observed six discretized emission energies (P_1 through P_6) ubiquitously across a broad range of hBN samples, that are of different layer thicknesses and prepared by various methods. The PL excitation, polarization and time-resolved measurements reveal fundamental photophysical properties of each discrete emission species (Summary in table S3). The boric acid etching at high temperatures preferentially converts P_3 into P_2, whereas water vapor etching reduces the number of active emitters evenly and simultaneously generates emitters. In addition, we have demonstrated that high-energy tip-

probe ultrasonication induces a new emission species P_7 that is not observed in hBN samples prepared by other methods. The observation of discretization and the chemical modulation is a cornerstone for understanding structural origins of hBN and further correlating a specific type of emitters, such as spin-active emission [49–53]. The facile chemical etching schemes should provide scalable post-processing routes for on-demand photonics of 2D materials.

Data availability statement

The data generated and/or analysed during the current study are not publicly available for legal/ethical reasons but are available from the corresponding author on reasonable request.

Author contributions

DK, SXL and MSS conceptualized the ideas, designed the experiments, and formulated the overarching research goals and aims. DK and SXL acquired, curated, and analysed the experimental data. DK, SXL and TI prepared all samples. TI, PL and DP assisted with the chemical etching experiments of hBN. VBK and ATL conducted XPS measurements. KSS assisted with the statistical analysis. AGR, XG, GH, VBK, YZ, MK, KSS, PL, SF, ZY, JW and DB assisted in the interpretation of the experimental results. DK, SXL and MSS wrote the manuscript, with input from all authors.

ORCID iDs

Xun Gong ⬡ https://orcid.org/0000-0003-4168-2768
Michael S Strano ⬡ https://orcid.org/0000-0003-2944-808X

References

[1] Sui M *et al* 2015 Gate-tunable topological valley transport in bilayer graphene *Nat. Phys.* **11** 1027–31
[2] Chen Y, Zou J, Campbell S J and Le Caer G 2004 Boron nitride nanotubes: pronounced resistance to oxidation *Appl. Phys. Lett.* **84** 2430–2
[3] Zhang Y, Shi Q, Liu Y, Wang Y, Meng Z, Xiao C, Deng K, Rao D and Lu R 2015 Hexagonal boron nitride with designed nanopores as a high-efficiency membrane for separating gaseous hydrogen from methane *J. Phys. Chem. C* **119** 19826–31
[4] Tran T T, Bray K, Ford M J, Toth M and Aharonovich I 2016 Quantum emission from hexagonal boron nitride monolayers *Nat. Nanotechnol.* **11** 37–41
[5] Aharonovich I, Englund D and Toth M 2016 Solid-state single-photon emitters *Nat. Photon.* **10** 631–41
[6] Kim S, Fröch J E, Christian J, Straw M, Bishop J, Totonjian D, Watanabe K, Taniguchi T, Toth M and Aharonovich I 2018 Photonic crystal cavities from hexagonal boron nitride *Nat. Commun.* **9** 2623
[7] Liu C-H, Clark G, Fryett T, Wu S, Zheng J, Hatami F, Xu X and Majumdar A 2017 Nanocavity integrated van der Waals heterostructure light-emitting tunneling diode *Nano Lett.* **17** 200–5
[8] Chejanovsky N *et al* 2016 Structural attributes and photodynamics of visible spectrum quantum emitters in hexagonal boron nitride *Nano Lett.* **16** 7037–45
[9] Hoese M, Reddy P, Dietrich A, Koch M K, Fehler K G, Doherty M W and Kubanek A 2020 Mechanical decoupling of quantum emitters in hexagonal boron nitride from low-energy phonon modes *Sci. Adv.* **6** eaba6038
[10] Hayee F *et al* 2020 Revealing multiple classes of stable quantum emitters in hexagonal boron nitride with correlated optical and electron microscopy *Nat. Mater.* **19** 534–9
[11] Tran T T, Zachreson C, Berhane A M, Bray K, Sandstrom R G, Li L H, Taniguchi T, Watanabe K, Aharonovich I and

Toth M 2016 Quantum emission from defects in single-crystalline hexagonal boron nitride *Phys. Rev. Appl.* **5** 2–9
[12] Zhang K, Feng Y, Wang F, Yang Z and Wang J 2017 Two dimensional hexagonal boron nitride (2D-hBN): synthesis, properties and applications *J. Mater. Chem. C* **5** 11992–2022
[13] Ngoc My Duong H, Nguyen M A P, Kianinia M, Ohshima T, Abe H, Watanabe K, Taniguchi T, Edgar J H, Aharonovich I and Toth M 2018 Effects of high-energy electron irradiation on quantum emitters in hexagonal boron nitride *ACS Appl. Mater. Interfaces* **10** 24886–91
[14] Tran T T, Elbadawi C, Totonjian D, Lobo C J, Grosso G, Moon H, Englund D R, Ford M J, Aharonovich I and Toth M 2016 Robust multicolor single photon emission from point defects in hexagonal boron nitride *ACS Nano* **10** 7331–8
[15] Fischer M, Caridad J M, Sajid A, Ghaderzadeh S, Ghorbani-Asl M, Gammelgaard L, Bøggild P, Thygesen K S, Krasheninnikov A V, Xiao S *et al* 2021 Controlled generation of luminescent centers in hexagonal boron nitride by irradiation engineering *Sci. Adv.* **7** eabe7138
[16] Xu Z Q *et al* 2018 Single photon emission from plasma treated 2D hexagonal boron nitride *Nanoscale* **10** 7957–65
[17] Gorbachev R V *et al* 2011 Hunting for monolayer boron nitride: optical and raman signatures *Small* **7** 465–8
[18] Mendelson N *et al* 2021 Identifying carbon as the source of visible single-photon emission from hexagonal boron nitride *Nat. Mater.* **20** 321–8
[19] Liu H *et al* 2022 Rational control on quantum emitter formation in carbon-doped monolayer hexagonal boron nitride *ACS Appl. Mater. Interfaces* **14** 3189–98
[20] Lyu C, Zhu Y, Gu P, Qiao J, Watanabe K, Taniguchi T and Ye Y 2020 Single-photon emission from two-dimensional hexagonal boron nitride annealed in a carbon-rich environment *Appl. Phys. Lett.* **117** 244002
[21] Abidi I H, Mendelson N, Tran T T, Tyagi A, Zhuang M, Weng L-T, Özyilmaz B, Aharonovich I, Toth M and Luo Z 2019 Selective defect formation in hexagonal boron nitride *Adv. Opt. Mater.* **7** 1900397
[22] Mendelson N, Xu Z Q, Tran T T, Kianinia M, Scott J, Bradac C, Aharonovich I and Toth M 2019 Engineering and tuning of quantum emitters in few-layer hexagonal boron nitride *ACS Nano* **13** 3132–40
[23] Dietrich A, Doherty M W, Aharonovich I and Kubanek A 2020 Solid-state single photon source with Fourier transform limited lines at room temperature *Phys. Rev. B* **101** 1–6
[24] Nikolay N, Mendelson N, Özelci E, Sontheimer B, Böhm F, Kewes G, Toth M, Aharonovich I and Benson O 2019 Direct measurement of quantum efficiency of single-photon emitters in hexagonal boron nitride *Optica* **6** 1084–8
[25] Wigger D *et al* 2019 Phonon-assisted emission and absorption of individual color centers in hexagonal boron nitride *2D Mater.* **6** 035006
[26] Museur L, Feldbach E and Kanaev A 2008 Defect-related photoluminescence of hexagonal boron nitride *Phys. Rev. B* **78** 155204
[27] Bourrellier R, Meuret S, Tararan A, Stéphan O, Kociak M, Tizei L H G and Zobelli A 2016 Bright UV single photon emission at point defects in h-BN *Nano Lett.* **16** 4317–21
[28] Hernández-Mínguez A, Lähnemann J, Nakhaie S, Lopes J M J and Santos P V 2018 Luminescent defects in a few-layer hBN film grown by molecular beam epitaxy *Phys. Rev. Appl.* **10** 044031
[29] Mendelson N, Doherty M, Toth M, Aharonovich I and Tran T T 2020 Strain-induced modification of the optical characteristics of quantum emitters in hexagonal boron nitride *Adv. Mater.* **32** 1908316
[30] Noh G, Choi D, Kim J-H, Im D-G, Kim Y-H, Seo H and Lee J 2018 Stark tuning of single-photon emitters in hexagonal boron nitride *Nano Lett.* **18** 4710–5

[31] Grosso G, Moon H, Lienhard B, Ali S, Efetov D K, Furchi M M, Jarillo-Herrero P, Ford M J, Aharonovich I and Englund D 2017 Tunable and high-purity room temperature single-photon emission from atomic defects in hexagonal boron nitride *Nat. Commun.* **8** 1–8

[32] Lazić S *et al* 2019 Dynamically tuned non-classical light emission from atomic defects in hexagonal boron nitride *Commun. Phys.* **2** 113

[33] Chejanovsky N, Kim Y, Zappe A, Stuhlhofer B, Taniguchi T, Watanabe K, Dasari D, Finkler A, Smet J H and Wrachtrup J 2017 Quantum light in curved low dimensional hexagonal boron nitride systems *Sci. Rep.* **7** 14758

[34] Proscia N V, Shotan Z, Jayakumar H, Reddy P, Cohen C, Dollar M, Alkauskas A, Doherty M, Meriles C A and Menon V M 2018 Near-deterministic activation of room-temperature quantum emitters in hexagonal boron nitride *Optica* **5** 1128–34

[35] Bourrellier R 2014 Nanometric resolved luminescence in h-BN flakes: excitons and stacking order *ACS Photon.* **1** 857–62

[36] Schell A W, Svedendahl M and Quidant R 2018 Quantum emitters in hexagonal boron nitride have spectrally tunable quantum efficiency *Adv. Mater.* **30** 1–5

[37] Wang Q *et al* 2018 Photoluminescence upconversion by defects in hexagonal boron nitride *Nano Lett.* **18** 6898–905

[38] Lin Y, Ling X, Yu L, Huang S, Hsu A L, Lee Y-H, Kong J, Dresselhaus M S and Palacios T 2014 Dielectric screening of excitons and trions in single-layer MoS$_2$ *Nano Lett.* **14** 5569–76

[39] Dietrich A, Bürk M, Steiger E S, Antoniuk L, Tran T T, Nguyen M, Aharonovich I, Jelezko F and Kubanek A 2018 Observation of Fourier transform limited lines in hexagonal boron nitride *Phys. Rev. B* **98** 081414

[40] Jungwirth N R, Calderon B, Ji Y, Spencer M G, Flatté M E and Fuchs G D 2016 Temperature dependence of wavelength selectable zero-phonon emission from single defects in hexagonal boron nitride *Nano Lett.* **16** 6052–7

[41] Exarhos A L, Hopper D A, Grote R R, Alkauskas A and Bassett L C 2017 Optical signatures of quantum emitters in suspended hexagonal boron nitride *ACS Nano* **11** 3328–36

[42] Jungwirth N R and Fuchs G D 2017 Optical absorption and emission mechanisms of single defects in hexagonal boron nitride *Phys. Rev. Lett.* **119** 1–6

[43] Xiao F, Naficy S, Casillas G, Khan M H, Katkus T, Jiang L, Liu H, Li H and Huang Z 2015 Edge-hydroxylated boron nitride nanosheets as an effective additive to improve the thermal response of hydrogels *Adv. Mater.* **27** 7196–203

[44] Blocquet M, Schoemaecker C, Amedro D, Herbinet O, Battin-Leclerc F and Fittschen C 2013 Quantification of OH and HO$_2$ radicals during the low-temperature oxidation of hydrocarbons by Fluorescence Assay by Gas Expansion technique *Proc. Natl Acad. Sci.* **110** 20014–7

[45] Zhi C Y, Bando Y, Terao T, Tang cc, Kuwahara H and Golberg D 2009 Chemically activated boron nitride nanotubes *Chem. Asian J.* **4** 1536–40

[46] Gong Y, Shi G, Zhang Z, Zhou W, Jung J, Gao W, Ma L, Yang Y, Yang S, You G *et al* 2014 Direct chemical conversion of graphene to boron-and nitrogen-and carbon-containing atomic layers *Nat. Commun.* **5** 1–8

[47] Weng Q *et al* 2017 Tuning of the optical, electronic, and magnetic properties of boron nitride nanosheets with oxygen doping and functionalization *Adv. Mater.* **29** 1–8

[48] Ashokkumar M 2011 The characterization of acoustic cavitation bubbles–an overview *Ultrason. Sonochem.* **18** 864–72

[49] Gottscholl A *et al* 2020 Initialization and read-out of intrinsic spin defects in a van der Waals crystal at room temperature *Nat. Mater.* **19** 540–5

[50] Gottscholl A, Diez M, Soltamov V, Kasper C, Sperlich A, Kianinia M, Bradac C, Aharonovich I and Dyakonov V 2022 Room temperature coherent control of spin defects in hexagonal boron nitride *Sci. Adv.* **7** eabf3630

[51] Gottscholl A, Diez M, Soltamov V, Kasper C, Krauße D, Sperlich A, Kianinia M, Bradac C, Aharonovich I and Dyakonov V 2021 Spin defects in hBN as promising temperature, pressure and magnetic field quantum sensors *Nat. Commun.* **12** 4480

[52] Fröch J E, Spencer L P, Kianinia M, Totonjian D D, Nguyen M, Gottscholl A, Dyakonov V, Toth M, Kim S and Aharonovich I 2021 Coupling spin defects in hexagonal boron nitride to monolithic bullseye cavities *Nano Lett.* **21** 6549–55

[53] Exarhos A L, Hopper D A, Patel R N, Doherty M W and Bassett L C 2019 Magnetic-field-dependent quantum emission in hexagonal boron nitride at room temperature *Nat. Commun.* **10** 1–8